Monthly Notices
of the
ROYAL ASTRONOMICAL SOCIETY

MNRAS **475,** 3577–3597 (2018)
Advance Access publication 2018 January 9

doi:10.1093/mnras/sty051

Early 2017 observations of TRAPPIST-1 with *Spitzer*

L. Delrez,[1]★ M. Gillon,[2] A. H. M. J. Triaud,[3] B.-O. Demory,[4] J. de Wit,[5] J. G. Ingalls,[6] E. Agol,[7,8]† E. Bolmont,[9,10] A. Burdanov,[2] A. J. Burgasser,[11] S. J. Carey,[6] E. Jehin,[2] J. Leconte,[12] S. Lederer,[13] D. Queloz,[1] F. Selsis[12] and V. Van Grootel[2]

[1]*Cavendish Laboratory, JJ Thomson Avenue, Cambridge CB3 0HE, UK*
[2]*Space Sciences, Technologies and Astrophysics Research (STAR) Institute, Université de Liège, Allée du 6 Août 19C, B-4000 Liège, Belgium*
[3]*School of Physics & Astronomy, University of Birmingham, Edgbaston, Birmingham B15 2TT, UK*
[4]*Center for Space and Habitability, University of Bern, Gesellschaftsstrasse 6, CH-3012 Bern, Switzerland*
[5]*Department of Earth, Atmospheric and Planetary Sciences, Massachusetts Institute of Technology, 77 Massachusetts Avenue, Cambridge, MA 02139, USA*
[6]*IPAC, California Institute of Technology, 1200 E California Boulevard, Mail Code 314-6, Pasadena, CA 91125, USA*
[7]*Astronomy Department, University of Washington, Seattle, WA 98195, USA*
[8]*NASA Astrobiology Institute's Virtual Planetary Laboratory, Seattle, WA 98195, USA*
[9]*IRFU, CEA, Université Paris-Saclay, F-91191 Gif-sur-Yvette, France*
[10]*Université Paris Diderot, AIM, Sorbonne Paris Cité, CEA, CNRS, F-91191 Gif-sur-Yvette, France*
[11]*Center for Astrophysics and Space Science, University of California San Diego, La Jolla, CA 92093, USA*
[12]*Laboratoire d'astrophysique de Bordeaux, Univ. Bordeaux, CNRS, B18N, Allée Geoffroy Saint-Hilaire, F-33615 Pessac, France*
[13]*NASA Johnson Space Center, 2101 NASA Parkway, Houston, TX 77058, USA*

Accepted 2017 December 31. Received 2017 December 21; in original form 2017 October 12

ABSTRACT

The recently detected TRAPPIST-1 planetary system, with its seven planets transiting a nearby ultracool dwarf star, offers the first opportunity to perform comparative exoplanetology of temperate Earth-sized worlds. To further advance our understanding of these planets' compositions, energy budgets, and dynamics, we are carrying out an intensive photometric monitoring campaign of their transits with the *Spitzer Space Telescope*. In this context, we present 60 new transits of the TRAPPIST-1 planets observed with *Spitzer*/Infrared Array Camera (IRAC) in 2017 February and March. We combine these observations with previously published *Spitzer* transit photometry and perform a global analysis of the resulting extensive data set. This analysis refines the transit parameters and provides revised values for the planets' physical parameters, notably their radii, using updated properties for the star. As part of our study, we also measure precise transit timings that will be used in a companion paper to refine the planets' masses and compositions using the transit timing variations method. TRAPPIST-1 shows a very low level of low-frequency variability in the IRAC 4.5-μm band, with a photometric RMS of only 0.11 per cent at a 123-s cadence. We do not detect any evidence of a (quasi-)periodic signal related to stellar rotation. We also analyse the transit light curves individually, to search for possible variations in the transit parameters of each planet due to stellar variability, and find that the *Spitzer* transits of the planets are mostly immune to the effects of stellar variations. These results are encouraging for forthcoming transmission spectroscopy observations of the TRAPPIST-1 planets with the *James Webb Space Telescope*.

Key words: techniques: photometric – stars: individual: TRAPPIST-1 – planetary systems.

1 INTRODUCTION

Small stars are beneficial for the discovery and study of exoplanets by transit methods (e.g. Nutzman & Charbonneau 2008; He, Triaud & Gillon 2017). For a given planet's size and irradiation, they offer deeper planetary transits and shorter orbital periods. The

★ E-mail: lcd44@cam.ac.uk
† Guggenheim Fellow.

seven Earth-sized worlds orbiting the nearby ultracool dwarf star TRAPPIST-1 (Gillon et al. 2016, 2017, hereafter G16 and G17, respectively) have become prime targets for the study of small planets beyond the Solar system, including the study of their atmospheres, owing to their transiting configuration combined with the infrared brightness ($K = 10.3$) and Jupiter-like size ($\sim 0.12\ R_\odot$) of their host star (Barstow & Irwin 2016; de Wit et al. 2016; Morley et al. 2017).

The TRAPPIST-1 planets have further importance. There are approximately three times as many M-dwarfs as FGK-dwarfs in the Milky Way (Kroupa 2001; Chabrier 2003; Henry et al. 2006), and small planets appear to surround M-dwarfs three to five times more frequently than Sun-like stars (e.g. Bonfils et al. 2013; Dressing & Charbonneau 2013, 2015). If this trend continues to the bottom of the main sequence (see He et al. 2017), the TRAPPIST-1 planets could well represent the most common Earth-sized planets in our Galaxy, which in itself would warrant special attention. TRAPPIST-1 also presents an interesting numerical and dynamical challenge; for example, assessing its stability on Gyr time-scales for orbital periods that have day to week time-scales (Tamayo et al. 2016, 2017).

A comparative study of the TRAPPIST-1 planets is aided by the fact that they all transit the same star. Because the knowledge of most planetary parameters (e.g. mass and radius) is dependent on knowing these parameters for their parent stars, it is often difficult to make accurate comparisons across systems. Although the parameters of the TRAPPIST-1 planets remain dependent on the parameters of their host star, we can nevertheless compare the planets to one another. Furthermore, the planets have emerged from the same nebular environment, have experienced a similar history in terms of irradiation (notably in the XUV range; Bourrier et al. 2017; O'Malley-James & Kaltenegger 2017; Wheatley et al. 2017), and similar volatile delivery and atmospheric sculpting via cometary impacts (Kral et al., submitted). Thus, any differences among the planets must be the result of distinctions in their development. One example would be the possible detection of O_2, which on Earth has biological origins but on other worlds can be produced abiologically through the photodissociation of water vapour and escape of hydrogen (e.g. Wordsworth & Pierrehumbert 2014; Bolmont et al. 2017). The presence of significant O_2 on only one of the seven planets would indicate a process particular to that planet, such as microbial respiration, with potentially far-reaching implications in humanity's search for life beyond the Earth.

To improve the characterization of the planets in the TRAPPIST-1 system, and prepare for exploration of their atmospheric properties with the upcoming *James Webb Space Telescope* (*JWST*) mission (Barstow & Irwin 2016; Morley et al. 2017), we are conducting an intensive, high-precision, space-based photometric monitoring campaign of the system with *Spitzer* (Exploration Programme ID 13067). The main goals of this programme are to improve the planets' transit parameters – notably to refine the determination of their radii – and to use the measured transit timing variations (TTVs) to constrain their masses and orbits (Agol et al. 2005; Holman & Murray 2005). Our *Spitzer* programme also aims to study the infrared variability of the host star and its possible impact on the future JWST observations, and to obtain first constraints on the presence of atmospheres around the planets by comparing their transit depths measured in the infrared by *Spitzer* to the ones measured at shorter wavelengths by other facilities (e.g. de Wit et al. 2016).

In this paper, we present observations gathered during the 2017 February–March window of visibility of the star by *Spitzer*. These new data more than double the number of transit events observed on TRAPPIST-1 with *Spitzer*. Section 2 describes the data and data reduction. In Section 3, we combine these observations with previous *Spitzer* transit photometry of TRAPPIST-1 presented in G17, and perform a global analysis that enables us to significantly improve the planets' transit parameters. We also use updated physical parameters for the star (Van Grootel et al. 2018), to revise the planets' physical parameters, notably their radii. In addition, we assess the low-frequency infrared variability of the star and its impact on our measured quantities. As part of our analysis, we also extract precise transit timings. Our TTV analysis of the current timing data set, including these new *Spitzer* timings, the resulting updated planetary masses, and our interpretations on the planets' composition and formation are presented in a separate companion paper (Grimm et al. 2018). In Section 4, we discuss our results, examining variability in the transit parameters over the breadth of the data set, and setting limits on wavelength-dependent transit depths for TRAPPIST-1b as a probe of its atmospheric properties. We summarize our results in Section 5.

2 OBSERVATIONS AND DATA REDUCTION

As part of our Warm *Spitzer* Exploration Science programme (ID 13067), *Spitzer* monitored 9, 16, 9, 6, 4, 3, and 1 new transit(s) of TRAPPIST-1b, -1c, -1d, -1e, -1f, -1g, and -1h, respectively, in the 4.5-μm channel of its Infrared Array Camera (IRAC, Fazio et al. 2004). Twelve additional transits of TRAPPIST-1b were also observed with IRAC in the 3.6-μm channel. All these observations were performed between 2017 February 18 and March 27. The corresponding data can be accessed using the *Spitzer* Heritage Archive.[1] The observations were obtained in subarray mode (32×32 pixels windowing of the detector) with an exposure time of 1.92 s. They were made without dithering (continuous staring) and in the pointing calibration and reference sensor peak-up mode (Ingalls et al. 2012), which maximizes the accuracy in the position of the target on the detector so as to minimize the so-called 'pixel phase effect' of IRAC indium antinomide arrays (e.g. Knutson et al. 2008). All the data were calibrated with the *Spitzer* pipeline S19.2.0, and delivered as cubes of 64 subarray images of 32×32 pixels (pixel scale = 1.2 arcsec).

Our photometric extraction was identical to that described in G17. After converting fluxes from MJy sr^{-1} to photon counts, we used the IRAF/DAOPHOT[2] software (Stetson 1987) to measure aperture photometry for the star within a circular aperture of 2.3 pixels. The apertures for each image were centred on the stellar point-spread function (PSF) by fitting to a 2D-Gaussian profile, which also yielded measurements of the PSF width along the x and y image coordinates. Images with discrepant measurements for the PSF centre, background flux, or source flux were discarded as described in Gillon et al. (2014). We then combined the measurements per cube of 64 images. The photometric errors were taken as the errors on the average flux measurements for each cube.

We complemented the resulting set of light curves with the *Spitzer* transit photometry previously published in G17, consisting of 16, 11, 5, 2, 3, 2, and 1 transit(s) of TRAPPIST-1b, -1c, -1d, -1e, -1f, -1g, and -1h, respectively, all observed with IRAC at 4.5 μm. We refer the reader to G17 and references therein for more details about these data.

[1] http://sha.ipac.caltech.edu

[2] IRAF is distributed by the National Optical Astronomy Observatory, which is operated by the Association of Universities for Research in Astronomy, Inc., under cooperative agreement with the National Science Foundation.

Our extensive *Spitzer* data set thus includes a total of 37, 27, 14, 8, 7, 5, and 2 transits of planets b, c, d, e, f, g, and h, respectively. A few of these light curves showed flare signatures for which we discarded the corresponding measurements.

3 DATA ANALYSIS

Our data analysis was divided into three steps. We first performed individual analyses of the transit light curves (Section 3.1) to select the optimal photometric model for each light curve, measure the transit timings, and assess the variability of the transit parameters for each planet due to stellar variability. We then performed a global analysis of the whole data set (Section 3.2) with the aim of improving our knowledge of the system parameters. Finally, we used our extensive *Spitzer* data set to assess the low-frequency infrared variability of the star in the IRAC 4.5-μm channel (Section 3.3).

Our individual and global data analyses were all carried out using the most recent version of the adaptive Markov Chain Monte Carlo (MCMC) code presented in Gillon et al. (2012, see also Gillon et al. 2014). We refer the reader to these papers and references therein for a detailed description of the MCMC algorithm and only describe below the aspects that are specific to the analyses presented here.

3.1 Individual analyses

We first converted each UT time of mid-exposure to the BJD_{TDB} time-scale, as described by Eastman, Siverd & Gaudi (2010). We then performed an individual model selection for each light curve, using the transit model of Mandel & Agol (2002) multiplied by a photometric baseline model, different for each light curve, aiming to represent the other astrophysical and instrumental effects at the source of photometric variations. A quadratic limb-darkening law was assumed for the star. For each light curve, we explored a large range of baseline models and selected the one that minimizes the Bayesian Information Criterion (BIC, Schwarz 1978). This led us to first include a linear or quadratic function of the x- and y-positions of the stellar PSF centre (as measured in the images by fitting a two-dimensional Gaussian profile) in the baseline model of every light curve to account for the pixel phase effect (e.g. Knutson et al. 2008). For some light curves, the modelling of this effect was improved by complementing the x- and y-polynomial with a numerical position model computed with the bi-linearly-interpolated sub-pixel sensitivity (BLISS) mapping method (Stevenson et al. 2012). The sampling of the position space (number of grid points) was selected so that at least five measurements were located in each sub-pixel box. We refer the reader to Gillon et al. (2014) for more details about the implementation of this approach in the MCMC code. We found that including a linear or quadratic function of the measured full width at half-maximum of the stellar PSF in the x- and/or y-directions resulted in a significant decrease in the BIC for most light curves (similar to Lanotte et al. 2014 and Demory et al. 2016). A polynomial of the logarithm of time was also required for some light curves to represent a sharp decrease of the detector response at the beginning of the observations (the so-called 'ramp effect', Knutson et al. 2008). Finally, a polynomial of time was also included in the baseline model for a fraction of the light curves to represent low-frequency signals likely related to the rotational variability of the star (see G16, Luger et al. 2017a, and Section 3.3).

For each individual analysis, the jump parameters of the MCMC, i.e. the parameters randomly perturbed at each step of the Markov chains, were as follows:

(i) The stellar mass $M_\star$, radius $R_\star$, effective temperature $T_{\rm eff}$, and metallicity [Fe/H]. We assumed the normal distributions $\mathcal{N}(0.0802, 0.0073^2)$ $M_\odot$, $\mathcal{N}(0.117, 0.0036^2)$ $R_\odot$, $\mathcal{N}(2559, 50^2)$ K, and $\mathcal{N}(0.04, 0.08^2)$ dex as respective prior probability distribution functions (PDFs) for these four parameters based on the values given in G17.

(ii) For each transit (some light curves cover several transits), the transit depth $dF = (R_p/R_\star)^2$, where R_p is the radius of the transiting planet, the transit impact parameter $b = a \cos i/R_\star$, where a is the orbital semimajor axis and i is the orbital inclination, the transit width W (defined as the duration from first to last contact), and the time of mid-transit T_0.

(iii) The linear combinations of the quadratic limb-darkening coefficients (u_1, u_2) in the considered bandpass, $c_1 = 2 \times u_1 + u_2$ and $c_2 = u_1 - 2 \times u_2$. For each bandpass, values and errors for u_1 and u_2 were interpolated for TRAPPIST-1 from the tables of Claret & Bloemen (2011) and the corresponding normal distributions were used as prior PDFs.

For these individual analyses, we kept the orbital period(s) of the relevant planet(s) fixed to the value(s) reported in G17 (for TRAPPIST-1b, c, d, e, f, g) and Luger et al. (2017a, for TRAPPIST-1h). As in G17, we assumed circular orbits for all the planets (eccentricity $e = 0$).

For each light curve, a preliminary MCMC analysis composed of one chain of 10 000 steps was first performed to estimate the correction factors CF to be applied to the photometric error bars, to account for both the over- or underestimation of the white noise of each measurement and the presence of correlated (red) noise in the data (see Gillon et al. 2012 and Appendix B1 for details). Then, a longer MCMC analysis was performed, composed of two chains of 100 000 steps, whose convergence was checked using the statistical test of Gelman & Rubin (1992).

Table A1 presents for each planet the transit timings, depths, and durations deduced from the individual analyses of its transit light curves. For each planet, we performed a linear regression of the measured *Spitzer* transit timings as a function of their epochs to derive an updated mean transit ephemeris (given in Table 1). We show individual depths and durations in Fig. 1 and see that in general, they are compatible to one another, epoch after epoch, following close to a normal distribution. Our individual uncertainties on the duration appear all slightly overestimated when we compare them to the mean of individual measurements. All planets have reduced chi-squared $\chi^2_r < 1$ except for TRAPPIST-1b at 3.6 μm, which has $\chi^2_r = 1.1$. The situation is different for the transit depths. TRAPPIST-1b (4.5 μm), -1c, -1d, -1f, and -1h have χ^2_r compatible with normal distribution, whereas TRAPPIST-1b (3.6 μm) has $\chi^2_r = 4.4$, TRAPPIST-1e has $\chi^2_r = 2.4$, and TRAPPIST-1g has $\chi^2_r = 4.3$. We discuss these dispersions later in the text (Section 4.2).

3.2 Global analysis

In a second phase, we carried out a global MCMC analysis of all the TRAPPIST-1 transits observed by *Spitzer* to improve the determination of the system parameters. We first performed a preliminary analysis, composed of one chain of 10 000 steps, to determine the correction factors CF to be applied to the error bars of each light curve (see Gillon et al. 2012 and Appendix B1 for details). With the corrected error bars, we then performed the final global analysis, consisting of two Markov chains of 100 000 steps. The jump parameters in our global analysis were as follows:

Table 1. Updated system parameters: median values and 1σ limits of the posterior PDFs derived from our global MCMC analysis.

Parameters	**Value**						
Star	**TRAPPIST-1**						
Mass[a], $M_\star$ ($M_\odot$)	0.0890 ± 0.0070						
Radius, $R_\star$ ($R_\odot$)	0.1210 ± 0.0030						
Density, $\rho_\star$ ($\rho_\odot$)	$51.1^{+1.2}_{-2.4}$						
Luminosity[a], $L_\star$ ($L_\odot$)	0.000522 ± 0.000019						
Effective temperature, $T_{\rm eff}$ (K)	2511 ± 37						
Metallicity[a], [Fe/H] (dex)	$+0.04 \pm 0.08$						
Limb-darkening coefficient[a], $u_{1,\,4.5\,\mu m}$	0.161 ± 0.019						
Limb-darkening coefficient[a], $u_{2,\,4.5\,\mu m}$	0.208 ± 0.021						
Limb-darkening coefficient[a], $u_{1,\,3.6\,\mu m}$	0.168 ± 0.020						
Limb-darkening coefficient[a], $u_{2,\,3.6\mu m}$	0.244 ± 0.021						
Planets	**b**	**c**	**d**	**e**	**f**	**g**	**h**
Number of transits observed	37	27	14	8	7	5	2
Period, P (d)	1.510 876 37 $\pm$0.000 000 39	2.421 807 46 $\pm$0.000 000 91	4.049 959 $\pm$0.000 078	6.099 043 $\pm$0.000 015	9.205 585 $\pm$0.000 016	12.354 473 $\pm$0.000 018	18.767953 $\pm$0.000080
Mid-transit time, $T_0 - 2450000$ (BJD_{TDB})	7322.516 54 $\pm$0.000 12	7282.808 79 $\pm$0.000 18	7670.142 27 $\pm$0.000 26	7660.379 10 $\pm$0.000 40	7671.394 70 $\pm$0.000 22	7665.350 84 $\pm$0.000 20	7662.55467 $\pm$0.00054
Transit depth at 4.5 μm, $dF_{4.5\,\mu m}$ (per cent)	0.7277 ± 0.0075	0.6940 ± 0.0068	0.3566 ± 0.0070	0.4802 ± 0.0094	0.634 ± 0.010	0.764 ± 0.011	0.346 ± 0.014
Transit depth at 3.6 μm $dF_{3.6\,\mu m}$ (per cent)	0.7070 ± 0.0086	–	–	–	–	–	-
Transit impact parameter, b ($R_\star$)	0.157 ± 0.075	0.148 ± 0.088	$0.08^{+0.10}_{-0.06}$	$0.240^{+0.056}_{-0.047}$	$0.337^{+0.040}_{-0.029}$	$0.406^{+0.031}_{-0.025}$	$0.392^{+0.039}_{-0.043}$
Transit duration, W (min)	36.19 ± 0.12	42.31 ± 0.14	$49.33^{+0.43}_{-0.32}$	55.92 ± 0.39	63.14 ± 0.36	68.53 ± 0.37	76.92 ± 0.96
Inclination, i (°)	89.56 ± 0.23	89.70 ± 0.18	$89.89^{+0.08}_{-0.15}$	$89.736^{+0.053}_{-0.066}$	$89.719^{+0.026}_{-0.039}$	$89.721^{+0.019}_{-0.026}$	89.796 ± 0.023
Semimajor axis, a (10^{-3} au)	$11.50^{+0.28}_{-0.25}$	$15.76^{+0.38}_{-0.34}$	$22.19^{+0.53}_{-0.48}$	$29.16^{+0.70}_{-0.63}$	$38.36^{+0.92}_{-0.84}$	46.7 ± 1.1	$61.7^{+1.5}_{-1.3}$
Scale parameter, $a/R_\star$	$20.56^{+0.16}_{-0.31}$	$28.16^{+0.22}_{-0.44}$	$39.68^{+0.32}_{-0.62}$	$52.13^{+0.41}_{-0.82}$	$68.6^{+0.6}_{-1.1}$	$83.5^{+0.7}_{-1.3}$	$110.3^{+0.9}_{-1.7}$
Irradiation, $S_{\rm p}$ ($S_\oplus$)	3.88 ± 0.22	2.07 ± 0.12	1.043 ± 0.060	0.604 ± 0.034	0.349 ± 0.020	0.236 ± 0.014	$0.135^{+0.078}_{-0.074}$
Equilibrium temperature[b] $T_{\rm eq}$ (K)	391.8 ± 5.5	334.8 ± 4.7	282.1 ± 4.0	246.1 ± 3.5	214.5 ± 3.0	194.5 ± 2.7	169.2 ± 2.4
Radius, $R_{\rm p}$ ($R_\oplus$)	1.127 ± 0.028	1.100 ± 0.028	0.788 ± 0.020	0.915 ± 0.025	1.052 ± 0.026	1.154 ± 0.029	0.777 ± 0.025

Notes. [a]Informative prior PDFs were assumed for these stellar parameters (see Section 3.2).
[b]Assuming a null Bond albedo.

(i) The stellar mass $M_\star$, radius $R_\star$, effective temperature $T_{\rm eff}$, and metallicity [Fe/H].

(ii) The linear combinations c_1 and c_2 of the quadratic limb-darkening coefficients (u_1, u_2) for each bandpass, defined as previously.

(iii) For the seven planets, the transit depth $dF_{4.5\mu m}$ at 4.5 μm, and the transit impact parameter b. The transit duration was not a jump parameter anymore in the global analysis, as it is uniquely defined for each planet by its orbital period, transit depth, and impact parameter, combined with the stellar mass and radius (Seager & Mallén-Ornelas 2003). This assumption neglects orbital eccentricity and transit duration variations, which may be justified due to the small eccentricities expected when migrating into Laplace resonances (Luger et al. 2017a), and the small amplitude of transit duration variations that is expected based on dynamical models.

(iv) For TRAPPIST-1b, the transit depth difference between the *Spitzer*/IRAC 3.6- and 4.5-μm channels: $ddF = dF_{3.6\mu m} - dF_{4.5\mu m}$.

(v) For the six inner planets, the TTV of each transit with respect to the mean transit ephemeris derived from the individual analyses (cf. Section 3.1).

(vi) For TRAPPIST-1h, the orbital period P, and the mid-transit time T_0.

This gives a total of 122 jump parameters for 19 258 data points. As previously, we assumed circular orbits for all the planets. For $M_\star$, we used a normal prior PDF based on the mass of 0.089 ± 0.007 $M_\odot$ semi-empirically derived by Van Grootel et al. (2018) for TRAPPIST-1 by combining a prior from stellar evolution models to a set of dynamical masses recently reported by Dupuy & Liu (2017) for a sample of equivalently classified ultracool dwarfs in astrometric binaries. We prefer here to assume this semi-empirical prior for the stellar mass rather than a purely theoretical one, like the one used previously in G16 and G17, as current stellar evolutionary models are known to underestimate the radii of some low-mass stars (e.g. Torres 2013; MacDonald & Mullan 2014, and references therein; see Van Grootel et al. 2018 for more details). We assumed

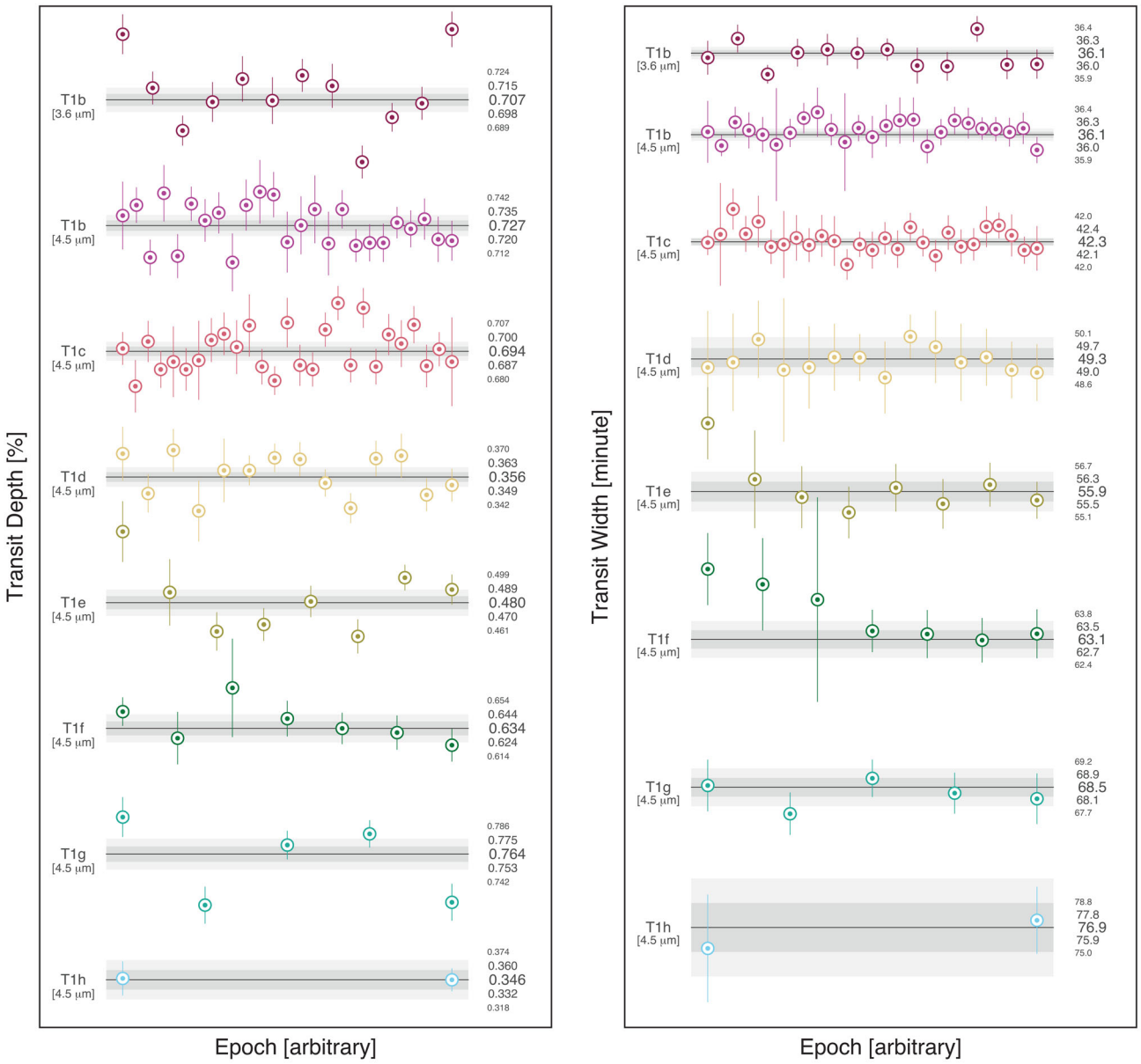

Figure 1. *Left:* Individual transit depth measurements for each of the events captured with *Spitzer*. The horizontal black line shows the median of the global MCMC posterior PDF (with its 1, and 2σ confidence, in shades of grey); the numeral values are also provided. Events are ranked in order of capture, left to right (but not linearly in time). *Right:* Similarly, but showing the duration of transit.

the same normal prior PDFs as previously for [Fe/H], and (u_1, u_2) for both bandpasses. Uniform non-informative prior distributions were assumed for the other jump parameters.

The convergence of the chains was again checked with the statistical test of Gelman & Rubin (1992). The Gelman–Rubin statistic was less than 1.11 for every jump parameter, measured across the two chains, indicating that the chains are converged. We also estimated the effective sample size of the chains ($N_{\rm eff}$) by computing the integrated autocorrelation length as defined in Gelman et al. (2013). We find a minimum $N_{\rm eff}$ of 27, with a median value of 118 over all parameters. Fig. 2 shows the autocorrelation function versus time lag for all 122 jump parameters.

The physical parameters of the system were deduced from the jump parameters at each step of the MCMC, so that their posterior PDFs could also be constructed. At each MCMC step, the value for $R_\star$ was combined with the updated luminosity reported by Van Grootel et al. (2018), $L_\star = (5.22 \pm 0.19) \times 10^{-4}$ $L_\odot$, based on their improved measurement of the star's parallax, to derive a value for $T_{\rm eff}$. For each planet, values for $R_{\rm p}$, a, and i, were deduced from the values for the stellar and transit parameters. Finally, values were also computed for the irradiation of each planet in Earth units and for their equilibrium temperatures, assuming a null Bond albedo.

Fig. 3 shows the detrended period-folded photometry for each planet with the corresponding best-fitting transit model, while Figs B1–B5 display binned residuals RMS versus bin size plots for the 78 light curves of our data set. Figs B6 and B7 show the cross-correlation plots and histograms of the posterior PDFs derived for the jump parameters of our global analysis, while Table 1

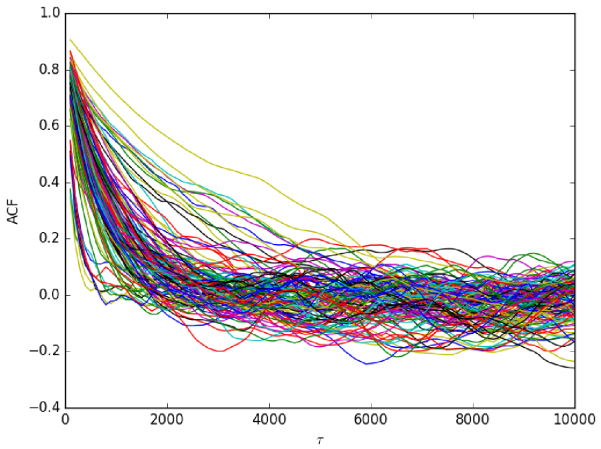

Figure 2. Autocorrelation function for all 122 jump parameters versus chain lag, τ.

presents the parameters derived for the system. We discuss these results in Section 4.

3.3 Stellar variability at 4.5 μm

Monitoring the stellar variability with *Spitzer* is rendered difficult because of two factors. First, half of the *Spitzer* observations analysed in this paper have been obtained in a time sparse mode, focusing on the transit windows of the seven TRAPPIST-1 planets. These sequences are short, up to 4 h long, which is not enough to sample the rotational period of the star. Secondly, we failed to consistently position the target on the detector's sweet spot, which systematically affects the measured flux at the ∼2 per cent level. Fig. 4 illustrates the absolute flux level measured for all TRAPPIST-1 AORs included in the present paper and the corresponding centroid locations on the detector. Two distinct areas can be seen because of pointing inaccuracies due to the target's large differential parallax between the Earth and *Spitzer*. To mitigate both caveats, we elect to conduct our variability analysis independently from the global fit presented above by only including the quasi-continuous sequence obtained over 21 d in 2016 September–October (G17). The corresponding centroid locations are clustered on bottom right of Fig. 4.

We performed the data reduction by computing the absolute fluxes of all AORs using a fixed aperture size of 3 pixels throughout the data set. A complication arose from the removal of the pixel-phase effect as TRAPPIST-1 fell 1 to 2 pixels away from the detector's sweet spot for which a high-resolution gain map exists (Ingalls et al. 2016). As no such map was available for our purpose, we calibrated the absolute photometry by using the data itself, using an implementation of the BLISS mapping algorithm (Stevenson et al. 2012). We found that the entire area over which the star fell is relatively extended (0.6 pixels along the x-axis and 0.5 pixels along the y-axis), which marginally limits the flux calibration accuracy. For the purposes of this stellar variability analysis, we discarded flares and removed transits based on the parameters deduced from our global analysis (Table 1). The photometric residuals are thus assumed to include signal from the star alone. We measured a photometric residual RMS of 0.11 per cent at a 123-s cadence. We performed a discrete Fourier analysis of the residuals that yielded a maximum at ∼10 d. The 3.30 ± 0.14-d rotation period found by Luger et al. (2017a, see also Vida et al. 2017) using 80-d continuous observations of visible K2 data, appears as a low-amplitude peak in our periodogram.

To obtain a more detailed view of the signal components, we further perform a wavelet analysis of the photometric residuals. For this purpose, we use the weighted wavelet Z-transform (WWZ) code presented in Foster (1996). The wavelet Z-statistic is computed as a function of both time and frequency, which gives further insights into the structure of the photometric residuals. The results of this analysis are shown in Fig. 5. We find that multiple peaks exist but that are of low amplitude. No signal is apparent around 3.3 d but the ∼10-d signature seems to persist across the entire window, albeit of low significance. The low-amplitude residual correlated noise could originate from imperfect instrumental systematic correction or from stellar noise. Assuming that the systematics correction we use is efficient, the wavelet analysis applied to the photometric residuals suggests that the star exhibits multiple active regions that evolve rapidly with time. The data at hand does not enable us to clearly identify the structure of the signal. We argue that long-term parallel monitoring of TRAPPIST-1 in the visible and infrared are desirable to better constrain its variability patterns.

We carried out an additional analysis of the power spectrum of TRAPPIST-1 using a correlated noise model described by a Gaussian process with a power spectrum defined as the sum of stochastically driven damped simple-harmonic oscillators, each with quality factor Q and frequency ω_0 (Foreman-Mackey et al. 2017). We fit the data with two components: a fixed $Q = 1/\sqrt{2}$ term which has a power spectrum describing variability similar to granulation, and a second $Q > >1$ term describing (quasi-)periodic variability, with a frequency initialized for a period of 3 d. We found that the amplitude of the large-Q term decreased to zero when optimizing the parameters of the Gaussian process, indicating that there is no evidence for quasi-periodic variability in the *Spitzer* 4.5-μm data set. We found that the 'granulation' term had a finite amplitude with a variance of 7×10^{-4}, and a frequency $\omega_0 = 22.45$ rad d^{-1}, corresponding to a characteristic damping time-scale of 0.28 d. Once the power spectrum was optimized, we subtracted off the Gaussian process estimate of the correlated noise component, and found that the normalized residuals follow a Gaussian, but slightly broader by a factor of 1.065, which is an additional argument for increasing the uncertainties on the data points with the correction factors, CF, as discussed above.

4 DISCUSSION

4.1 Updated system parameters

We have more than doubled the number of transit events observed with *Spitzer* on TRAPPIST-1 with respect to what has been presented in G17. Our global analysis refines the planets' transit depths (at 4.5 μm) by factors up to 2.8 (TRAPPIST-1e) and their transit durations by factors up to 2.8 (TRAPPIST-1h), and also slightly improves the precision of the physical parameters derived for the planets. An important point to outline is that in G16 and G17 our global analysis assumed an informative prior on the stellar mass and radius – and thus on the stellar density – based on stellar evolution models. In this new analysis, no informative prior was assumed for the stellar radius, and the stellar density was only constrained by the shape of the transits of the seven planets (Seager & Mallén-Ornelas 2003). Furthermore, our assumed prior on the stellar mass was here not only based on stellar physics computations but also on empirical data (see Section 3.2 and Van Grootel et al. 2018). We thus consider our updated planetary parameters presented in Table 1 not only more precise than those reported in G17, but also more accurate because they are less model-dependent. We compare

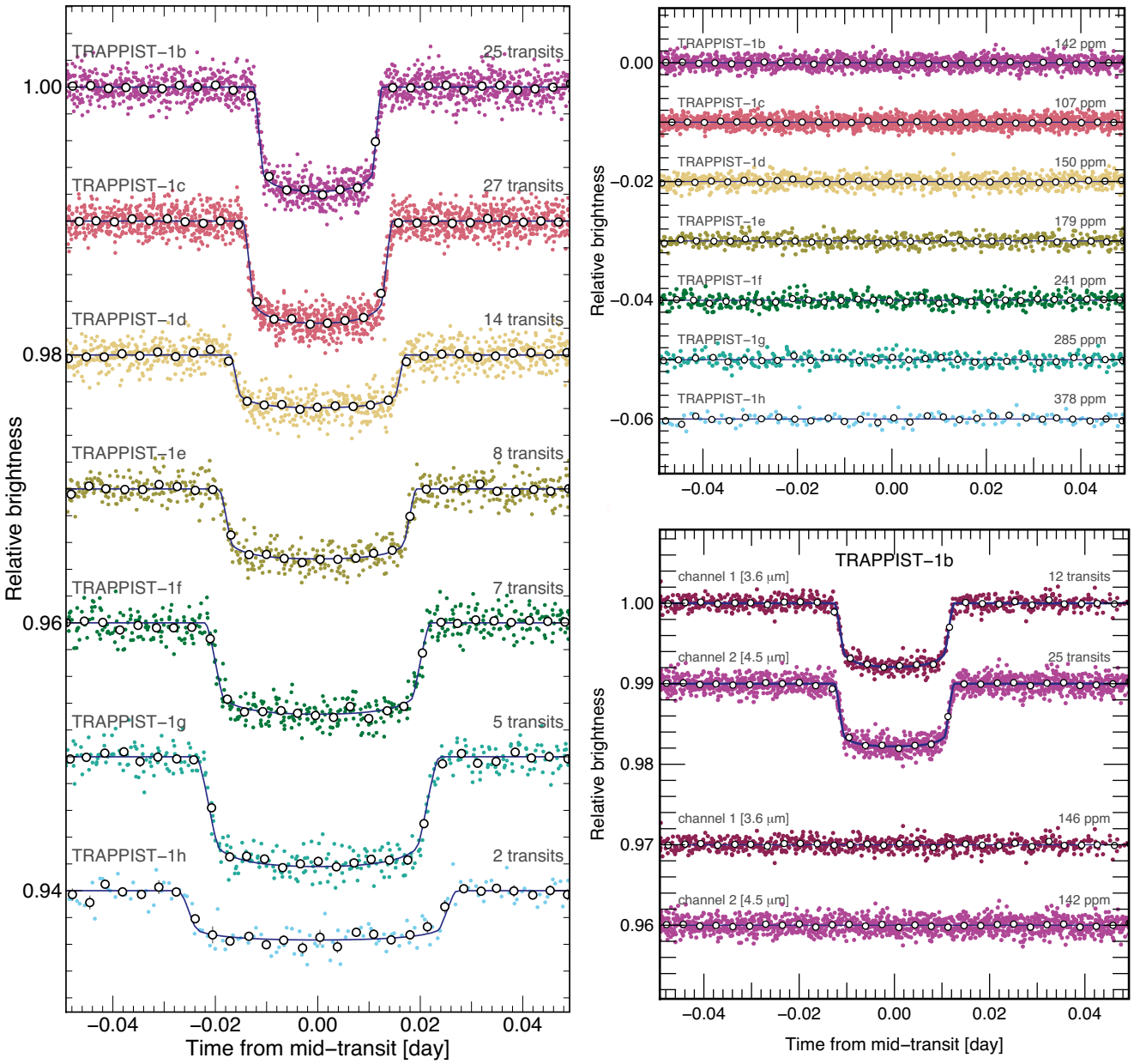

Figure 3. *Left:* Period-folded photometric measurements obtained by *Spitzer* at 4.5 μm near the transits of planets TRAPPIST-1b to TRAPPIST-1h, corrected for the measured TTVs. Coloured dots show the unbinned measurements; open circles depict 5-min-binned measurements for visual clarity. The best-fitting transit models are shown as coloured lines. The number of transits that were observed to produce these combined curves is written on the plot. *Top right:* Corresponding residuals. The RMS of the residuals (5-min bins) is indicated over each planet. *Bottom right:* Similar to other panels, only for TRAPPIST-1b at 3.6 μm (channel 1) and 4.5 μm (channel 2).

some of these quantities to Solar system objects and the rest of the small exoplanet population in Fig. 6.

4.2 Variability of the transit parameters

As reported in Section 3.3, we do not find any significant (quasi-)periodic signal in the IRAC 4.5-μm band related to the rotation of TRAPPIST-1. Rotational variability has however been previously detected by Luger et al. (2017a) in the *K2* passband, at the level of few per cent and with a period of ∼3.3 d. This periodic photometric variability indicates that inhomogeneities of the stellar surface (spots) move in and out of view as the star rotates. Luger, Lustig-Yaeger & Agol (2017b) recently demonstrated that the orbital planes of the TRAPPIST-1 planets are aligned to $<0.3^\circ$ at 90 per cent confidence. Together, the planets cover at least 56 per cent of a hemisphere when they transit (shadowed area in Fig. 7), notably the low and intermediate latitudes at which we find spots on the Sun (e.g. Miletskii & Ivanov 2009). We could therefore expect the planets to cross some stellar spots during their transits. Such occulted spots would affect the transit profile in a way that would depend on their size, contrast, and distribution across the planetary chord, and would tend to make the transit shallower. Unocculted spots, i.e. stellar spots that are not crossed during planetary transits, would have the opposite effect, making the transit deeper by

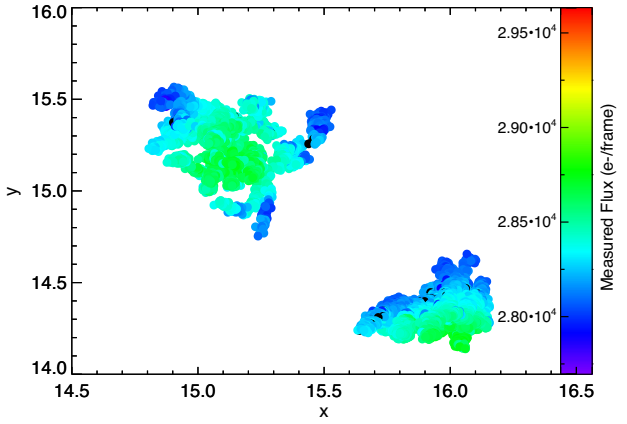

Figure 4. TRAPPIST-1 *Spitzer*/IRAC raw photometric fluxes collected from all 66 AORs taken between 2016 and March 2017 and the corresponding centroid locations on the detector.

diminishing the overall flux from the star while leaving the surface brightness along the transit chord unchanged. Because of stellar spots, either occulted or unocculted, we could thus expect to detect variations in the planets' transit depths as a function of time.

As noted in Section 3.1, the transit depths derived from the individual analyses generally follow a normal distribution for each planet, except TRAPPIST-1b at 3.6 μm, TRAPPIST-1e, and TRAPPIST-1g, each of which show some outliers. It is common knowledge that transit parameters derived from a single transit light curve can be significantly affected by systematics (e.g. Gillon et al. 2012). The global analysis of an extensive set of transit light curves, which assumes one unique transit profile for all the transit light curves (of a same planet), allows a better separation of the actual transit signal from the correlated noise and the derivation of robust transit parameters. To better assess the possible variations in the transit depth of each planet, we computed for each of its transits the

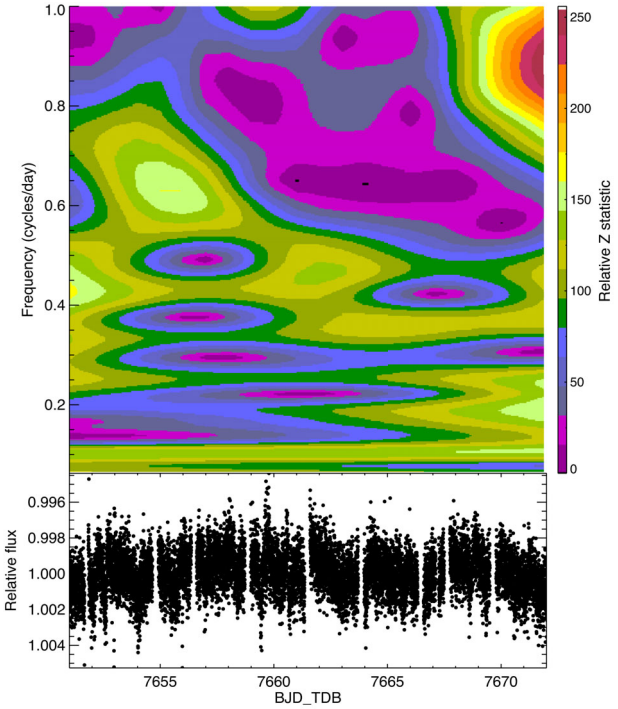

Figure 5. Wavelet diagram (*top*) of the photometric residuals (*bottom*).

median values of the photometric residuals in transit and out of transit, using for this purpose the photometric residuals from the global analysis. These median values, together with the median absolute deviations, are given for each transit in Table B1. A significant difference between the in-transit and out-of-transit medians of the photometric residuals for a given transit would indicate a variation in its depth compared to the planet's transit depth derived from the global analysis. However, the in-transit and out-of-transit medians

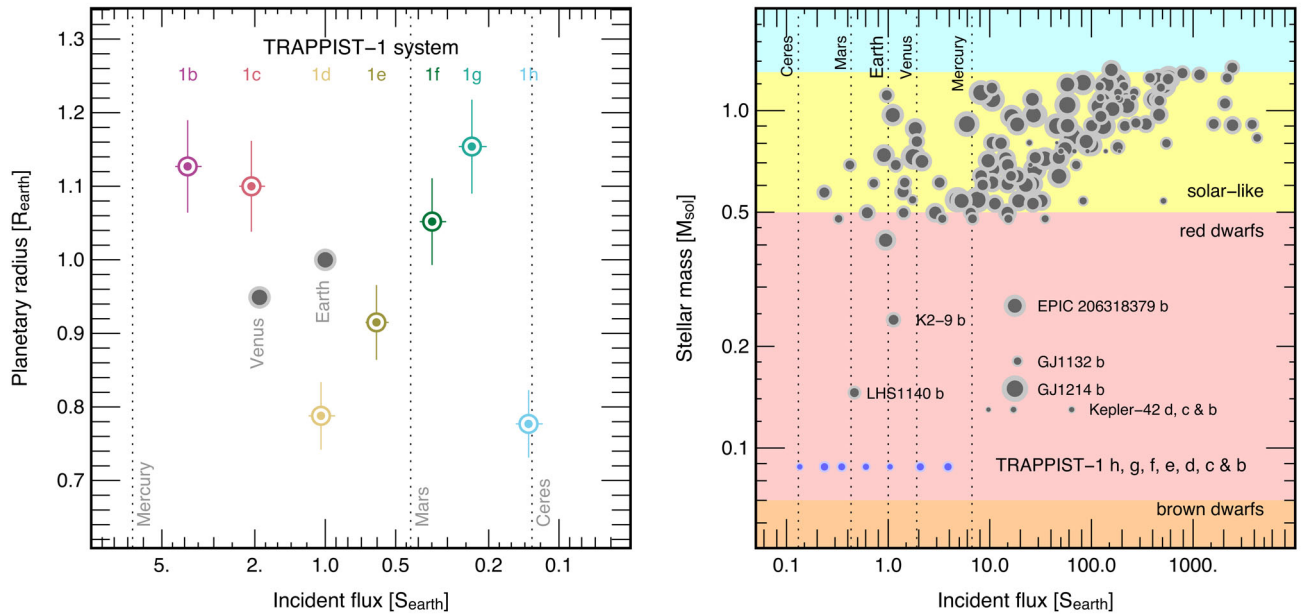

Figure 6. Updates on diagrams shown in G16 and G17. *Left:* Planetary radii as a function of incident flux. *Right:* Planet population shown ordered by stellar-host mass as a function of incident flux. Only planets with radii $<2R_\oplus$ are represented. The dots size increases linearly with radius.

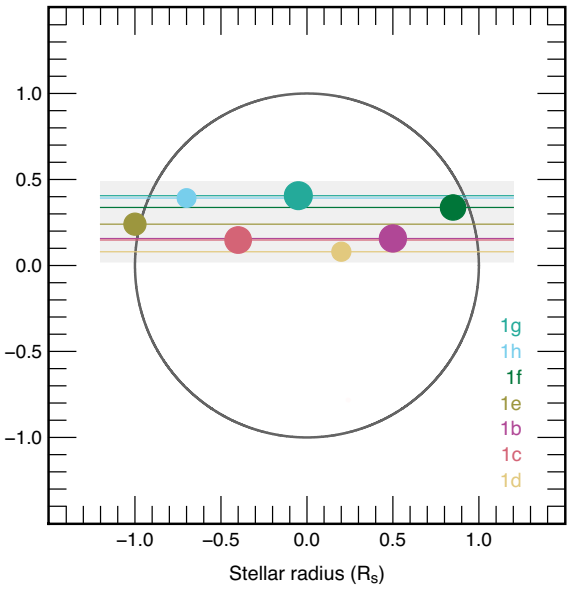

Figure 7. Representation of the star, and of the planets that transit it, using impact parameters and transit depths from Table 1. The planets cover a minimum area of ∼56 per cent of an hemisphere. Planetary position on its chord is arbitrary.

are compatible within 1 sigma for all transits of all planets. This test reveals that the variability seen for some planets (TRAPPIST-1b at 3.6 μm, TRAPPIST-1e, and TRAPPIST-1g) in the transit depths derived from the individual analyses is likely not physical but rather caused by systematic effects – which are better disentangled from the planetary signals in the global analysis.

In this context, it is worth noting that instrumental systematics are stronger at 3.6 μm than at 4.5 μm and thus require more complex baseline models, which can introduce some biases in the transit parameters derived from a single light curve. This might explain the increased scatter of TRAPPIST-1b's individual transit depths at 3.6 μm. For TRAPPIST-1e, we note that only the first transit in Fig. 1 (epoch -1) shows a discrepant transit depth. This transit was actually observed over two different consecutive AORs, which might have introduced a bias in its measured depth. As for TRAPPIST-1g, a visual inspection of the global analysis' residuals for the two transits with discrepant transit depths (second and fifth transits in Fig. 1, corresponding to epochs 0 and 14, respectively) does not reveal any obvious structures or spot-crossings. The origin of these two outliers thus remains unclear. Additional transit observations of this planet at higher SNR are needed to better assess the possible variability of its transit depth.

Overall, *Spitzer* transits of TRAPPIST-1 planets thus appear to be mostly immune to the effects of stellar variability. There are several reasons why this may happen:

(i) Considering the very low level of low-frequency photometric variability shown by TRAPPIST-1 at 4.5 μm, unocculted spots may not have a significant impact on the planets' transit depths. Using the simple model of Berta et al. (2011, see their equations 8 and 9) to estimate the expected amplitude of transit depth variations at 4.5 μm due to unocculted spots based on the stellar variability measured in that band, we indeed find amplitudes lower than 100 ppm for all the planets. This is smaller than the error bars on the individual transit depths. We note however that this estimate is only a lower limit to the possible amplitude of transit depth variations due to unocculted spots. Indeed, the rotational variability of the star reflects only the non-axisymmetric component of the stellar surface inhomogeneities. The axisymmetric component does not contribute to the measured stellar variability and its effect is thus not included in our estimate, while it is also expected to affect the planets' transit depths.

(ii) The periodic variability detected in the *K2* passband may be caused by high-latitude spots that do not cross the planets' chords, explaining the non-detection of spot-crossing events. Evidence for such high-latitude spots has been reported for some mid- and late-M dwarfs (see e.g. Barnes et al. 2015). We note however that these objects are usually young ($\lesssim$1 Gyr), while TRAPPIST-1 is a rather old system (7.6 ± 2.2 Gyr, Burgasser & Mamajek 2017).

(iii) Spot-crossing events may not produce detectable effects on the *Spitzer* transit light curves due to the reduced spot-to-photosphere contrast in the IRAC passbands (see e.g. Ballerini et al. 2012). A practical example of this effect was presented by Fraine et al. (2014), who reported simultaneous *Kepler* and *Spitzer* transit photometry of the Neptune-sized planet HAT-P-11b orbiting an active K4 dwarf. While some spot-crossing events are clearly visible in the *Kepler* optical photometry, they are undetected in the photometry obtained concurrently with *Spitzer* at 4.5 μm.

4.3 Transmission spectrum of TRAPPIST-1b

A transmission spectrum can be severely affected by both occulted and unocculted stellar spots (e.g. Jordán et al. 2013; McCullough et al. 2014; Rackham et al. 2017). To extract a proper transmission spectrum, a planet needs to cover a part of the stellar surface that has a spectrum that is representative of the whole disc. We are in a privileged position with TRAPPIST-1 as the planets cross over a quarter of the entire stellar surface, and more than half of a hemisphere. Unless spots never intersect transit chords, the planets will cross over a representative fraction of the star, and the transmission spectra measured for the TRAPPIST-1 planets should be robust measures of their atmospheres (Barstow & Irwin 2016; de Wit et al. 2016; Morley et al. 2017).

Our global data analysis yields a marginal transit depth difference of +208 ± 110 ppm for TRAPPIST-1b between the *Spitzer*/IRAC 4.5- and 3.6-μm channels, the transit being slightly deeper at 4.5 μm than at 3.6 μm (Table 1). If confirmed, this transit depth variation would imply that TRAPPIST-1b's atmosphere significantly exceeds its equilibrium temperature (392 K assuming a null Bond albedo, Table 1). A deeper transit depth at 4.5 μm would be best explained by atmospheric CO_2, which has a prominent absorption feature around 4.2 μm (see e.g. Kaltenegger & Traub 2009). The most favourable scenario to enhance such a signature requires no other opacity source across the IRAC 3.6-μm channel than the extended wing of the 4.2-μm absorption band of CO_2. In such a case, the variation in transit depth is approximately equivalent to five scale heights (H) at medium spectral resolution (see e.g. Kaltenegger & Traub 2009; de Wit & Seager 2013) and 2H when binned over IRAC's channels. TRAPPIST-1b's scale height would thus be larger or equal to approximately 52 km [208 ppm $= ((R_p + 2H)/R_\star)^2 - (R_p/R_\star)^2$]. For comparison, the Earth's atmospheric scale height is 8.5 km, while that of Venus is 15.9 km.[3] This lower limit on the planet atmospheric scale height can be translated into a lower limit on its atmospheric temperature owing to assumptions of its atmospheric

[3] https://nssdc.gsfc.nasa.gov/planetary/factsheet/

mean molecular mass, μ, and surface gravity, g. Planet b's surface gravity is approximately 8 m s^{-2} (Grimm et al. 2018). Under the present assumption that no strong absorber affects the 3.6-μm band, the background gas cannot be water or methane – both exhibit absorption features in this band – implying that the atmosphere must have a large μ (e.g. 28 u.m.a. if dominated by N_2). Under such a favourable scenario for the CO_2 feature, TRAPPIST-1 b's atmosphere would require an average temperature above 1400 K–more than three times larger than its estimated equilibrium temperature. On the other hand, if water dominates its atmosphere, this would lead to two counter-balancing effects: (1) a decrease of the mean molecular weight and (2) a transit depth variation between the two IRAC channels of no more than a scale height due to water absorption at 3.3 μm. This would yield an atmospheric scale height larger than ∼100 km and an average atmospheric temperature above ∼1800 K. Other opacity sources, such as clouds or hazes, would require an even larger scale height and atmospheric temperature to support such a variation in transit depth between the two IRAC channels. Therefore, if confirmed, such hint of variability would be indicative of a surprisingly large atmospheric temperature for TRAPPIST-1b.

As demonstrated recently by Deming & Sheppard (2017), transit measurements of a planet transiting an M-dwarf can be affected by a resolution-linked bias (RLB) effect, which acts to decrease the apparent amplitude of an absorption feature from the planetary atmosphere. This is due to the complex line structure exhibited by M-dwarfs which creates a flux-leakage effect at low to medium spectral resolution wherein the stellar flux does not entirely cancel out in the ratio of in- to out-of-transit flux. We estimated the amplitude of the RLB effect on the transit depth difference expected for TRAPPIST-1b between the IRAC 4.5-μm and 3.6-μm channels assuming different atmospheric scenarios, namely H_2-, H_2O-, N_2-, and CO_2-rich atmospheres (de Wit et al. 2016). For TRAPPIST-1 spectrum, we used the PHOENIX/BT-Settl model with $T_{\rm eff}$/log g/[M/H] of 2500 K/5.5/0.0 (Allard, Homeier & Freytag 2012). We find a maximal RLB effect of ∼115 ppm over a ∼2400 ppm absorption feature of methane in a H_2-rich atmosphere, which corresponds to a dampening of the methane absorption feature by ∼5 per cent. Although the amplitude of the effect in this case is comparable to the uncertainty on our measured transit depth difference, it is not relevant for the interpretation of our measurements as the hint of feature detected between the two IRAC channels is not of the order of ∼2400 ppm. We find amplitudes ranging from only a few ppm to 30 ppm for the other atmospheric scenarios. The marginal difference in transit depth that we measure between both IRAC bands is thus not expected to be significantly affected by the RLB effect.

5 CONCLUSIONS

In this work, we presented 60 new transits of the TRAPPIST-1 planets observed with *Spitzer*/IRAC in early 2017. We performed a global analysis of the entire *Spitzer* data set gathered so far, which enabled us to refine the transit parameters and to provide revised values for the planets' physical parameters, notably their radii, using updated properties for the host star. As part of this study, we also extracted precise transit timings that will be instrumental for TTV studies of the system, to be presented in a companion paper. In addition, we found that the star shows a very low level of low-frequency variability in the IRAC 4.5-μm channel. We did not detect any evidence of a (quasi-)periodic signal related to stellar rotation and found that the planets' transit depths measured with *Spitzer* are mostly not affected by stellar variability. Finally, we also found for TRAPPIST-1b a marginal transit depth difference of $+208 \pm 110$ ppm between the IRAC 4.5- and 3.6-μm channels. If confirmed, this transit depth variation could indicate the presence of CO_2 in the planet's atmosphere as well as a surprisingly large atmospheric temperature. Together, these results improve our understanding of this remarkable system and help prepare the detailed atmospheric characterization of its planets with *JWST*.

ACKNOWLEDGEMENTS

We thank E. Gillen for interesting discussions and valuable suggestions. This work is based in part on observations made with the *Spitzer Space Telescope*, which is operated by the Jet Propulsion Laboratory, California Institute of Technology, under a contract with NASA. This work was partially supported by a grant from the Simons Foundation (PI Queloz, grant number 327127). The research leading to these results also received funding from the European Research Council (ERC) under the FP/2007-2013 ERC grant agreement no. 336480, and under the H2020 ERC grant agreement no. 679030; and from an Action de Recherche Concertée (ARC) grant, financed by the Wallonia-Brussels Federation. LD acknowledges support from the Gruber Foundation Fellowship. VVG and MG are F.R.S.-FNRS Research Associates. EJ is F.R.S.-FNRS Senior Research Associate. B-OD acknowledges support from the Swiss National Science Foundation in the form of a SNSF Professorship (PP00P2_163967). EB acknowledges funding by the European Research Council through ERC grant SPIRE 647383. AJB acknowledges funding support from the US–UK Fulbright Scholarship programme.

REFERENCES

Agol E., Steffen J., Sari R., Clarkson W., 2005, MNRAS, 359, 567
Allard F., Homeier D., Freytag B., 2012, Phil. Trans. R. Soc. A, 370, 2765
Ballerini P., Micela G., Lanza A. F., Pagano I., 2012, A&A, 539, A140
Barnes J. R., Jeffers S. V., Jones H. R. A., Pavlenko Y. V., Jenkins J. S., Haswell C. A., Lohr M. E., 2015, ApJ, 812, 42
Barstow J. K., Irwin P. G. J., 2016, MNRAS, 461, L92
Berta Z. K., Charbonneau D., Bean J., Irwin J., Burke C. J., Désert J.-M., Nutzman P., Falco E. E., 2011, ApJ, 736, 12
Bolmont E., Selsis F., Owen J. E., Ribas I., Raymond S. N., Leconte J., Gillon M., 2017, MNRAS, 464, 3728
Bonfils X. et al., 2013, A&A, 549, A109
Bourrier V. et al., 2017, A&A, 599, L3
Burgasser A. J., Mamajek E. E., 2017, ApJ, 845, 110
Chabrier G., 2003, PASP, 115, 763
Claret A., Bloemen S., 2011, A&A, 529, A75
Cubillos P., Harrington J., Loredo T. J., Lust N. B., Blecic J., Stemm M., 2017, AJ, 153, 3
de Wit J., Seager S., 2013, Science, 342, 1473
de Wit J. et al., 2016, Nature, 537, 69
Deming D., Sheppard K., 2017, ApJ, 841, L3
Demory B.-O., Gillon M., Madhusudhan N., Queloz D., 2016, MNRAS, 455, 2018
Dressing C. D., Charbonneau D., 2013, ApJ, 767, 95
Dressing C. D., Charbonneau D., 2015, ApJ, 807, 45
Dupuy T. J., Liu M. C., 2017, ApJS, 231, 15
Eastman J., Siverd R., Gaudi B. S., 2010, PASP, 122, 935
Fazio G. G. et al., 2004, ApJS, 154, 10
Foreman-Mackey D., 2016, J. Open Source Softw., 1, 24
Foreman-Mackey D., Agol E., Ambikasaran S., Angus R., 2017, AJ, 154, 220
Foster G., 1996, AJ, 112, 1709
Fraine J. et al., 2014, Nature, 513, 526
Gelman A., Rubin D. B., 1992, Stat. Sci., 7, 457

Gelman A., Carlin J., Stern H., Dunson D., Vehtari A., Rubin D., 2013, Bayesian Data Analysis, 3rd edn. Chapman & Hall/CRC Texts in Statistical Science, Taylor & Francis
Gillon M. et al., 2012, A&A, 542, A4
Gillon M. et al., 2014, A&A, 563, A21
Gillon M. et al., 2016, Nature, 533, 221 (G16)
Gillon M. et al., 2017, Nature, 542, 456 (G17)
Grimm S. et al., 2018, A&A, in press
He M. Y., Triaud A. H. M. J., Gillon M., 2017, MNRAS, 464, 2687
Henry T. J., Jao W.-C., Subasavage J. P., Beaulieu T. D., Ianna P. A., Costa E., Méndez R. A., 2006, AJ, 132, 2360
Holman M. J., Murray N. W., 2005, Science, 307, 1288
Ingalls J. G., Krick J. E., Carey S. J., Laine S., Surace J. A., Glaccum W. J., Grillmair C. C., Lowrance P. J., 2012, in Clampin M. C., Fazio G. G., MacEwen H. A., Oschmann J. M. Jr, eds, Proc. SPIE Conf. Ser. Vol. 8442, Space Telescopes and Instrumentation 2012: Optical, Infrared, and Millimeter Wave. SPIE, Bellingham, p. 84421Y
Ingalls J. G. et al., 2016, AJ, 152, 44
Jordán A. et al., 2013, ApJ, 778, 184
Kaltenegger L., Traub W. A., 2009, ApJ, 698, 519
Knutson H. A., Charbonneau D., Allen L. E., Burrows A., Megeath S. T., 2008, ApJ, 673, 526
Kroupa P., 2001, MNRAS, 322, 231
Lanotte A. A. et al., 2014, A&A, 572, A73
Luger R. et al., 2017a, Nat. Astron., 1, 0129
Luger R., Lustig-Yaeger J., Agol E., 2017b, ApJ, 851, 94
MacDonald J., Mullan D. J., 2014, ApJ, 787, 70
Mandel K., Agol E., 2002, ApJ, 580, L171
McCullough P. R., Crouzet N., Deming D., Madhusudhan N., 2014, ApJ, 791, 55
Miletskii E. V., Ivanov V. G., 2009, Astron. Rep., 53, 857
Morley C. V., Kreidberg L., Rustamkulov Z., Robinson T., Fortney J. J., 2017, ApJ, 850, 121
Nutzman P., Charbonneau D., 2008, PASP, 120, 317
O'Malley-James J. T., Kaltenegger L., 2017, MNRAS, 469, L26
Rackham B. et al., 2017, ApJ, 834, 151
Schwarz G., 1978, Ann. Stat., 6, 461
Seager S., Mallén-Ornelas G., 2003, ApJ, 585, 1038
Stetson P. B., 1987, PASP, 99, 191
Stevenson K. B. et al., 2012, ApJ, 754, 136
Tamayo D. et al., 2016, ApJ, 832, L22
Tamayo D., Rein H., Petrovich C., Murray N., 2017, ApJ, 840, L19
Torres G., 2013, Astron. Nachr., 334, 4
Van Grootel V. et al., 2018, ApJ, 853, 30
Vida K., Kővári Z., Pál A., Oláh K., Kriskovics L., 2017, ApJ, 841, 124
Wheatley P. J., Louden T., Bourrier V., Ehrenreich D., Gillon M., 2017, MNRAS, 465, L74
Winn J. N. et al., 2008, ApJ, 683, 1076
Wordsworth R., Pierrehumbert R., 2014, ApJ, 785, L20

APPENDIX A: RESULTS FROM THE INDIVIDUAL ANALYSES

Table A1. Median values and 1σ limits of the posterior PDFs deduced for the timings, depths, and durations of the transits from their individual analyses.

Planet	Epoch	Channel	T_0 (BJD$_{\rm TDB}$ − 2450000)	eT_0	dF (per cent)	ed$F$	W (min)	eW
b	78	2	7440.365 14	0.00035	0.742	0.048	36.30	1.20
	86	2	7452.452 28	0.00014	0.757	0.025	35.76	0.40
	93	2	7463.028 47	0.00019	0.682	0.025	36.68	0.59
	218	2	7651.887 43	0.00022	0.774	0.040	36.36	0.69
	219	2	7653.398 09	0.00026	0.684	0.031	36.19	0.68
	220	2	7654.909 08	0.00084	0.759	0.024	35.80	2.20
	222	2	7657.931 29	0.00020	0.735	0.030	36.26	0.54
	223	2	7659.441 44	0.00017	0.746	0.029	36.84	0.58
	224	2	7660.952 05	0.00033	0.675	0.041	37.07	0.95
	225	2	7662.463 58	0.00020	0.757	0.036	36.39	0.60
	226	2	7663.974 92	0.00070	0.776	0.045	35.90	1.90
	227	2	7665.485 09	0.00017	0.772	0.032	36.45	0.50
	228	2	7666.995 67	0.00025	0.704	0.043	36.10	0.81
	229	2	7668.506 68	0.00030	0.728	0.041	36.54	0.81
	230	2	7670.017 66	0.00034	0.751	0.048	36.75	0.89
	231	2	7671.528 76	0.00030	0.702	0.045	36.78	0.86
	318	2	7802.975 57	0.00016	0.751	0.027	35.73	0.65
	320	2	7805.996 97	0.00016	0.699	0.023	36.29	0.50
	321	2	7807.507 31	0.00017	0.703	0.026	36.75	0.52
	322	1	7809.018 22	0.00017	0.801	0.028	36.01	0.65
	324	2	7812.040 38	0.00020	0.703	0.027	36.64	0.59
	325	2	7813.551 21	0.00014	0.732	0.022	36.43	0.43
	326	1	7815.062 75	0.00017	0.724	0.023	36.76	0.53
	327	1	7816.573 35	0.00011	0.663	0.021	35.36	0.35
	328	2	7818.083 82	0.00015	0.723	0.026	36.41	0.46
	329	1	7819.594 78	0.00017	0.704	0.028	36.21	0.53
	330	1	7821.105 50	0.00020	0.737	0.032	36.33	0.60
	332	2	7824.127 30	0.00018	0.737	0.029	36.29	0.55
	333	1	7825.638 13	0.00018	0.706	0.033	36.19	0.60
	334	1	7827.149 95	0.00012	0.742	0.023	36.33	0.42
	335	1	7828.660 42	0.00024	0.727	0.031	35.70	0.69
	336	2	7830.170 87	0.00021	0.708	0.032	36.44	0.60
	338	1	7833.192 57	0.00018	0.618	0.023	35.67	0.55
	339	1	7834.703 98	0.00016	0.682	0.020	37.14	0.49
	340	2	7836.214 40	0.00017	0.706	0.028	35.59	0.50
	341	1	7837.725 26	0.00014	0.702	0.023	35.74	0.56
	342	1	7839.236 69	0.00017	0.808	0.025	35.76	0.56
c	70	2	7452.334 70	0.00015	0.698	0.023	42.28	0.48
	71	2	7454.756 72	0.00066	0.644	0.037	42.60	2.00
	152	2	7650.923 95	0.00023	0.708	0.029	43.59	0.79
	153	2	7653.345 53	0.00024	0.668	0.026	42.62	0.69
	154	2	7655.767 85	0.00040	0.679	0.050	43.10	1.00
	155	2	7658.189 63	0.00024	0.668	0.030	42.11	0.66
	156	2	7660.611 68	0.00051	0.681	0.056	42.20	1.30
	157	2	7663.032 92	0.00028	0.710	0.031	42.46	0.88
	158	2	7665.455 19	0.00025	0.719	0.030	42.18	0.65
	159	2	7667.877 29	0.00031	0.700	0.038	42.54	0.81
	160	2	7670.298 69	0.00035	0.731	0.044	42.34	0.96
	215	2	7803.497 47	0.00020	0.672	0.025	41.42	0.59
	216	2	7805.91882	0.00017	0.652	0.020	42.21	0.48
	217	2	7808.34123	0.00023	0.735	0.035	41.98	0.71
	218	2	7810.76273	0.00019	0.674	0.029	42.45	0.62
	219	2	7813.18456	0.00024	0.668	0.024	42.02	0.72
	220	2	7815.60583	0.00017	0.725	0.024	42.88	0.55
	221	2	7818.02821	0.00020	0.763	0.024	42.28	0.53
	222	2	7820.45019	0.00022	0.674	0.024	41.76	0.60
	223	2	7822.871 88	0.000 21	0.756	0.028	42.67	0.66
	224	2	7825.293 88	0.000 22	0.672	0.025	42.12	0.66
	225	2	7827.715 13	0.000 22	0.718	0.029	42.21	0.62
	226	2	7830.137 13	0.000 26	0.705	0.033	42.90	0.79
	227	2	7832.558 88	0.000 15	0.732	0.026	42.95	0.49
	228	2	7834.981 20	0.000 25	0.673	0.030	42.56	0.81
	229	2	7837.402 80	0.000 17	0.697	0.024	41.98	0.52
	230	2	7839.824 15	0.000 31	0.679	0.063	42.05	0.86

Table A1 – *continued*

Planet	Epoch	Channel	T_0 [BJD$_{TDB}$ − 2450000]	eT_0	dF [per cent]	ed$F$	W [min]	eW
d	−4	2	7653.942 61	0.000 51	0.390	0.038	49.00	2.20
	−3	2	7657.992 20	0.000 63	0.333	0.027	49.20	1.90
	−2	2	7662.042 84	0.000 51	0.395	0.030	50.10	1.50
	−1	2	7666.091 40	0.001 30	0.308	0.043	48.90	2.80
	0	2	7670.141 98	0.000 66	0.366	0.045	49.00	1.60
	33	2	7803.790 83	0.000 49	0.366	0.021	49.40	1.30
	34	2	7807.840 32	0.000 30	0.384	0.020	49.39	0.91
	35	2	7811.891 16	0.000 50	0.382	0.024	48.60	1.40
	36	2	7815.940 64	0.000 30	0.348	0.019	50.21	0.85
	37	2	7819.990 50	0.000 50	0.312	0.021	49.80	1.40
	38	2	7824.041 85	0.000 67	0.383	0.025	49.20	1.50
	39	2	7828.090 82	0.000 43	0.387	0.031	49.40	1.10
	40	2	7832.140 36	0.000 37	0.331	0.023	48.90	1.10
	41	2	7836.191 71	0.000 42	0.345	0.023	48.80	1.10
e	−1	2	7654.278 62	0.000 49	0.582	0.043	58.60	1.40
	0	2	7660.380 16	0.000 78	0.495	0.047	56.40	1.90
	24	2	7806.757 58	0.000 41	0.439	0.027	55.70	1.20
	25	2	7812.857 01	0.000 34	0.449	0.023	55.10	1.00
	26	2	7818.955 10	0.000 30	0.482	0.022	56.07	0.92
	27	2	7825.053 08	0.000 35	0.432	0.024	55.44	0.96
	28	2	7831.152 06	0.000 27	0.516	0.018	56.19	0.85
	29	2	7837.249 80	0.000 25	0.499	0.021	55.58	0.71
f	−2	2	7652.985 79	0.000 32	0.658	0.020	65.90	1.40
	−1	2	7662.187 47	0.000 40	0.620	0.037	65.30	1.80
	0	2	7671.392 79	0.000 72	0.692	0.070	64.70	4.00
	15	2	7809.475 54	0.000 27	0.648	0.025	63.47	0.82
	16	2	7818.682 71	0.000 32	0.634	0.022	63.35	0.93
	17	2	7827.886 69	0.000 30	0.628	0.024	63.11	0.86
	18	2	7837.103 22	0.000 32	0.610	0.023	63.36	0.95
g	−1	2	7652.994 81	0.000 30	0.817	0.028	68.60	1.00
	0	2	7665.351 51	0.000 28	0.691	0.026	67.49	0.82
	12	2	7813.606 84	0.000 23	0.777	0.020	68.88	0.72
	13	2	7825.961 12	0.000 20	0.793	0.019	68.30	0.79
	14	2	7838.306 55	0.000 28	0.695	0.026	68.08	0.98
h	0	2	7662.554 67	0.000 54	0.348	0.024	76.1	2.1
	9	2	7831.466 25	0.000 47	0.346	0.016	77.2	1.3

APPENDIX B: GLOBAL ANALYSIS: SUPPLEMENTARY MATERIAL

B1 Binned residuals RMS versus bin size plots

Figs B1–B5 show the RMS versus bin size plots for the 78 *Spitzer*/IRAC light curves of our data set, made using the `bin_rms` routine of the `MC`[3] open-source PYTHON package (Cubillos et al. 2017). For each light curve, the RMS of the binned residuals, RMS$_N$, is shown as a black curve for bin sizes (i.e. the mean number N of points in each bin) ranging from one to half the data size. The uncertainty of RMS$_N$ (grey error bars) is computed as $\sigma_{\rm RMS} = {\rm RMS}_N/\sqrt{2M}$ (see Cubillos et al. 2017 for the derivation), where M is the number of bins. The red curve shows the expected RMS σ_N in the absence of correlated noise, given by (Winn et al. 2008):

$$\sigma_N = \frac{\sigma_1}{\sqrt{N}}\sqrt{\frac{M}{M-1}}, \tag{B1}$$

where σ_1 is the RMS of the unbinned residuals. The saw-tooth look of this red curve arises from the discreet change in M, which becomes more significant as N increases.

As mentioned in Section 3, the possible presence of correlated noise in the data is accounted for in our analyses via correction factors CF that we applied to the photometric error bars of each light curve before performing the final analyses. For each light curve, CF is the product of two contributions, β_w and β_r. On one side, β_w represents the under- or overestimation of the white noise of each measurement. It is computed as the ratio between the RMS of the unbinned residuals and the mean photometric error. On the other side, β_r allows to account for possible correlated noise present in the light curve, and is calculated as

$$\beta_r = \frac{{\rm RMS}_N}{\sigma_N} \tag{B2}$$

$$= \frac{\sigma_N}{\sigma_1}\sqrt{\frac{N(M-1)}{M}}. \tag{B3}$$

The largest value obtained with different bin sizes is kept as β_r.

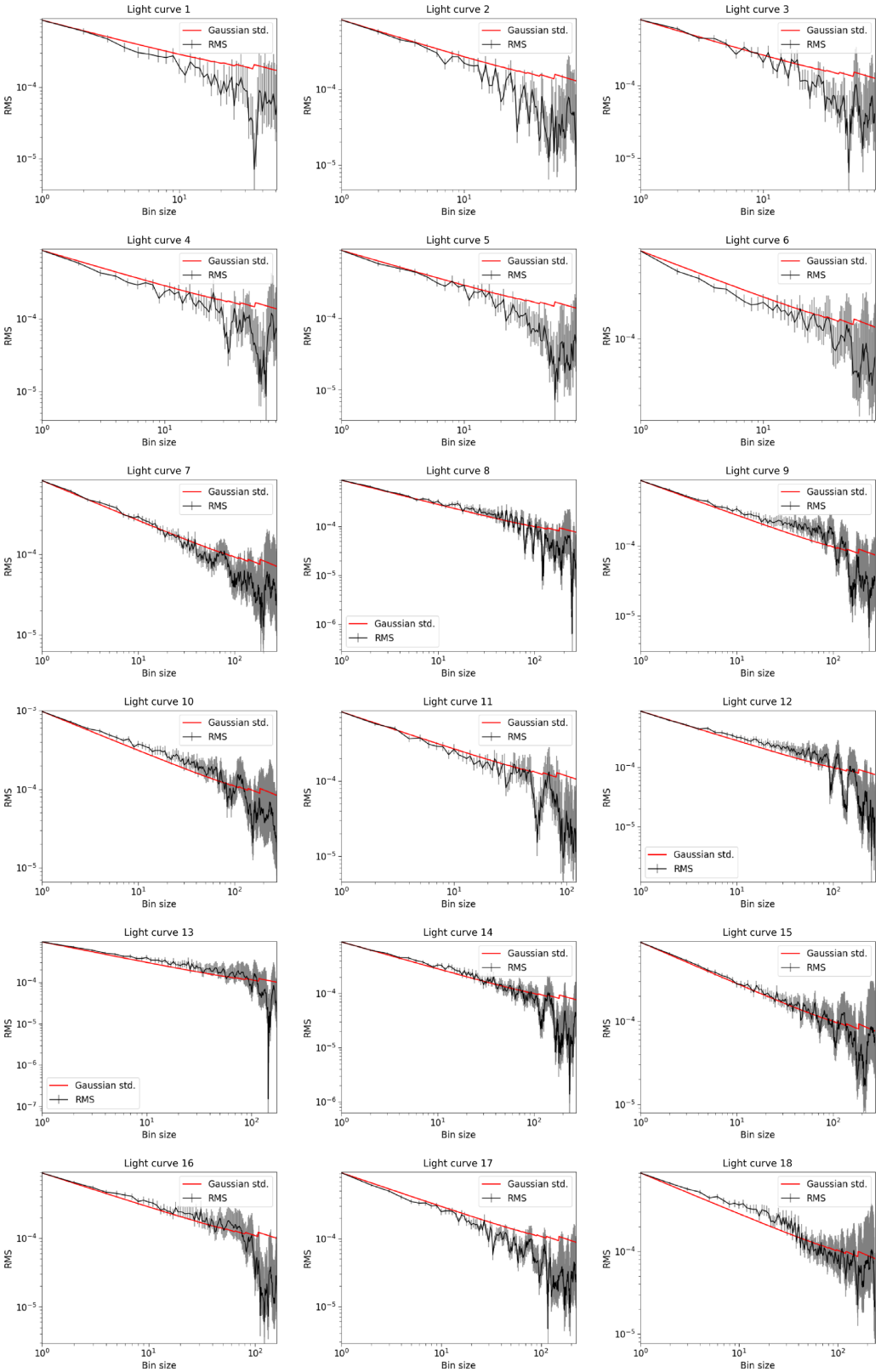

Figure B1. Binned residuals RMS (black curves with grey error bars) versus bin size for the first 18 *Spitzer*/IRAC light curves. The red curves are the expected RMS for Gaussian noise.

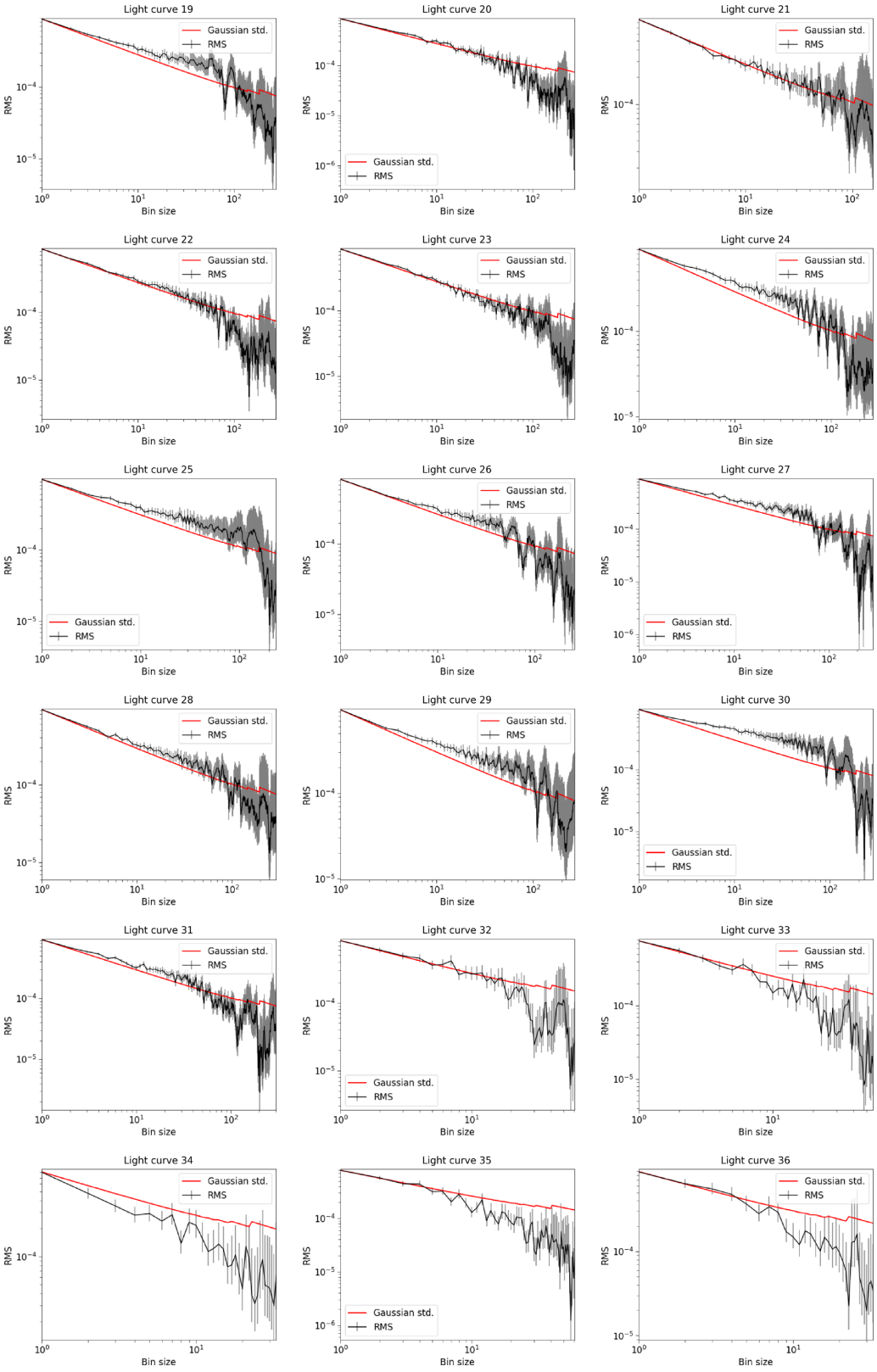

Figure B2. Same as Fig. B1, but for light curves 19–36.

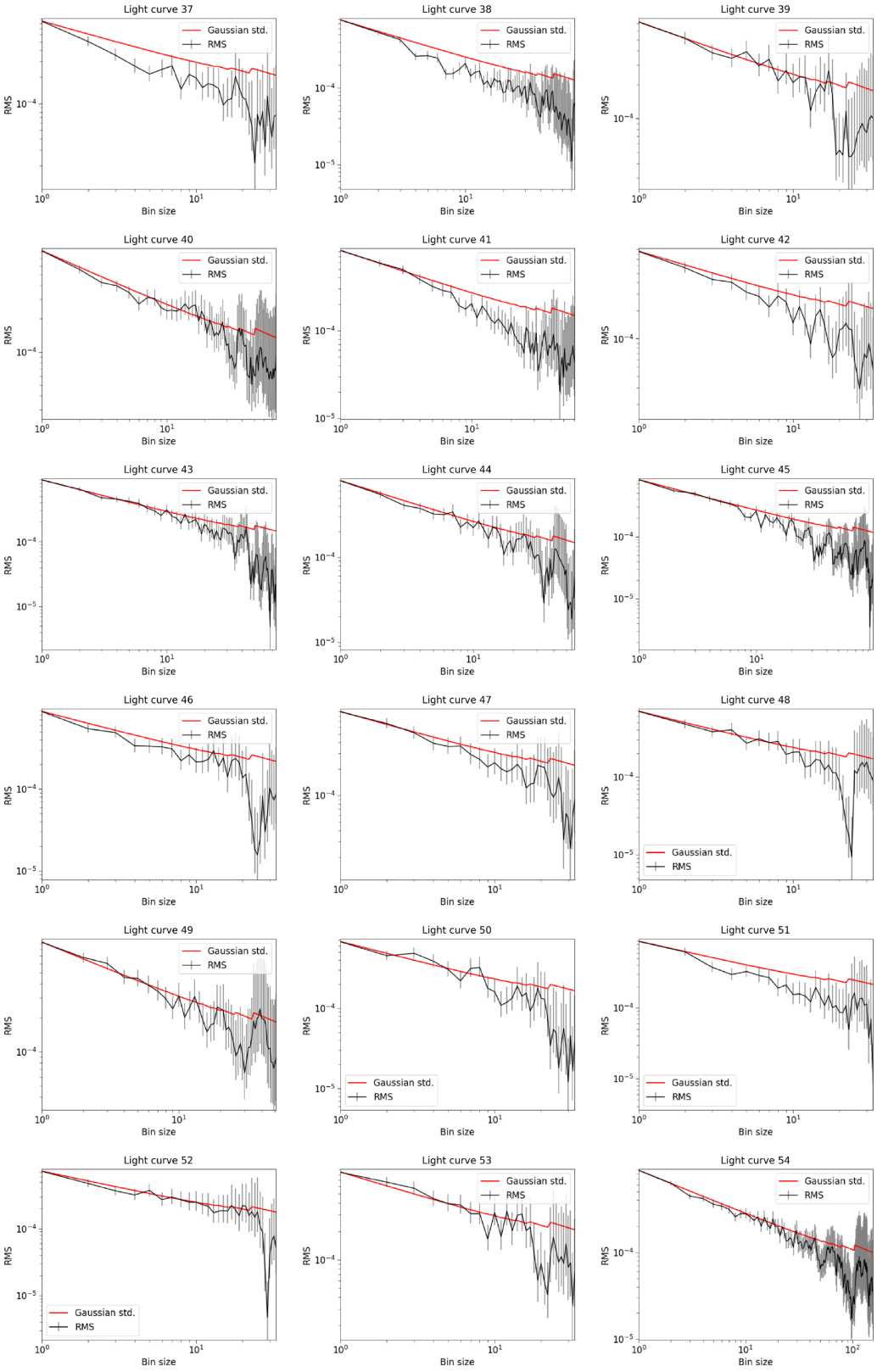

Figure B3. Same as Fig. B1, but for light curves 37–54.

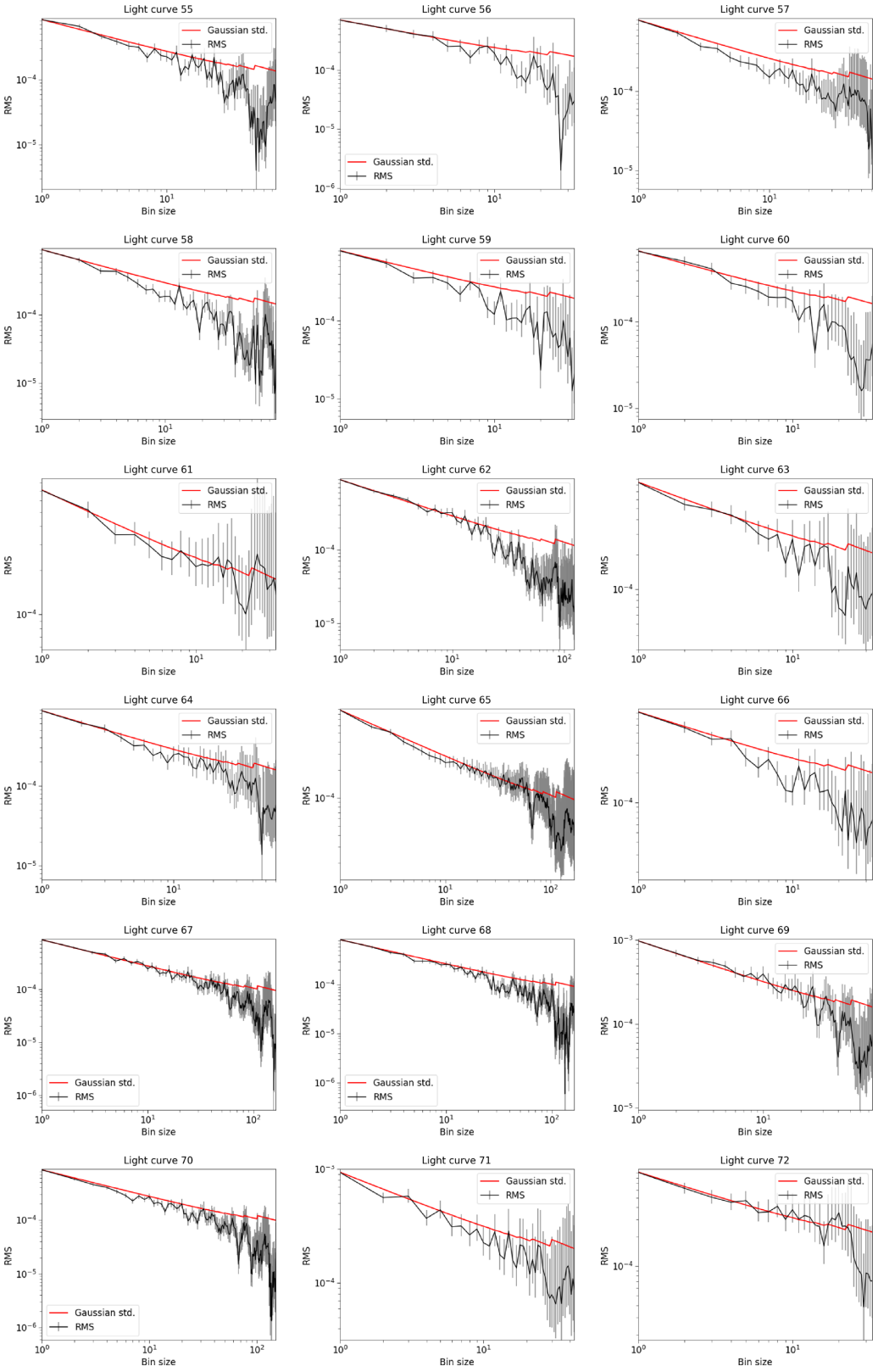

Figure B4. Same as Fig. B1, but for light curves 55–72.

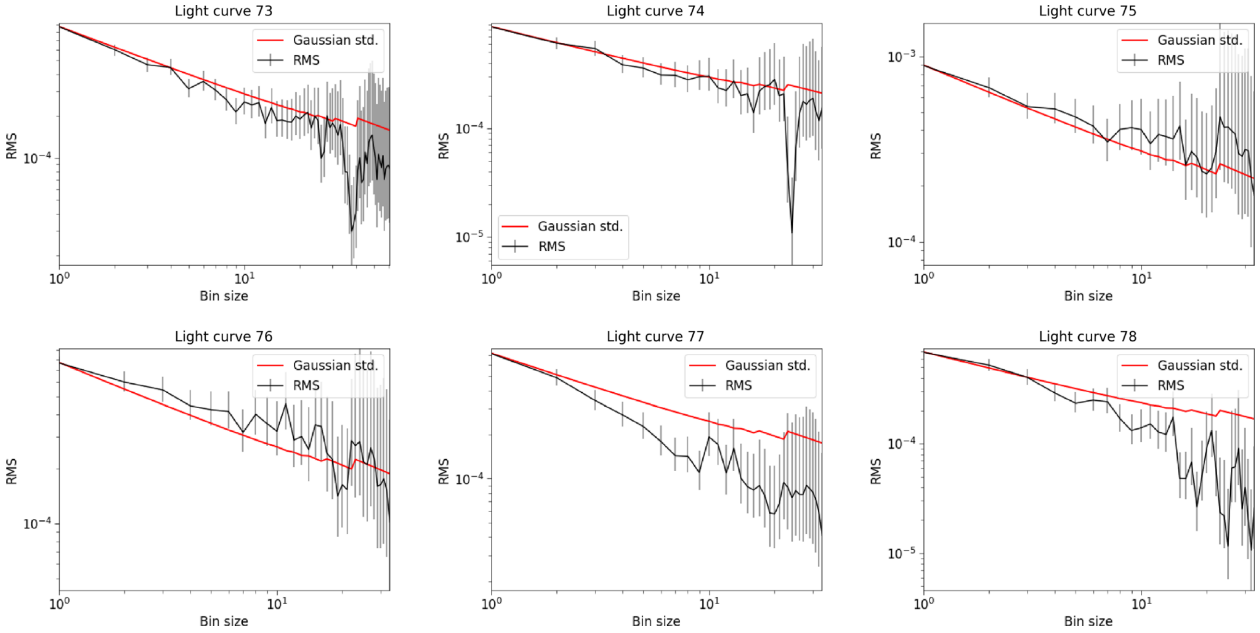

Figure B5. Same as Fig. B1, but for light curves 73–78.

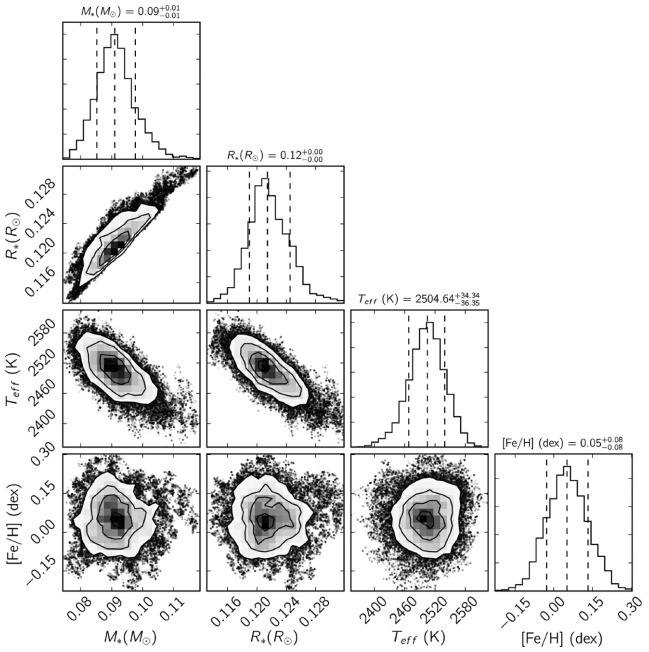

Figure B6. Cross-correlation plots and histograms of the posterior PDFs deduced for the stellar parameters from our global analysis.

B2 Cross-correlation plots of the posterior PDFs

Fig. B6 shows the cross-correlation of the posterior parameters for the star from the global analysis made using `corner.py` (Foreman-Mackey 2016). Since the transit duration–period relation constrains the density of the star strongly, the mass and radius are strongly correlated. As the luminosity prior is strongly constrained, the uncertainty in radius is anticorrelated with the effective temperature. The metallicity correlates weakly with the other stellar parameters.

Fig. B7 shows the correlations between transit impact parameter and depth. As a common density for the star was used for all the transits, the impact parameters are strongly correlated as they anticorrelate with the transit durations, while the durations are well constrained by the data, and as zero eccentricity was assumed for the planet orbits. The depths correlate with the impact parameters as larger impact parameters have transit chords with lower surface brightness (due to limb-darkening), requiring a larger planet to cause the same transit depth.

The limb-darkening parameters and transit times correlate weakly with all of the other parameters, so we have not included these in the cross-correlation plots.

B3 Median values of the residuals in and out of transit

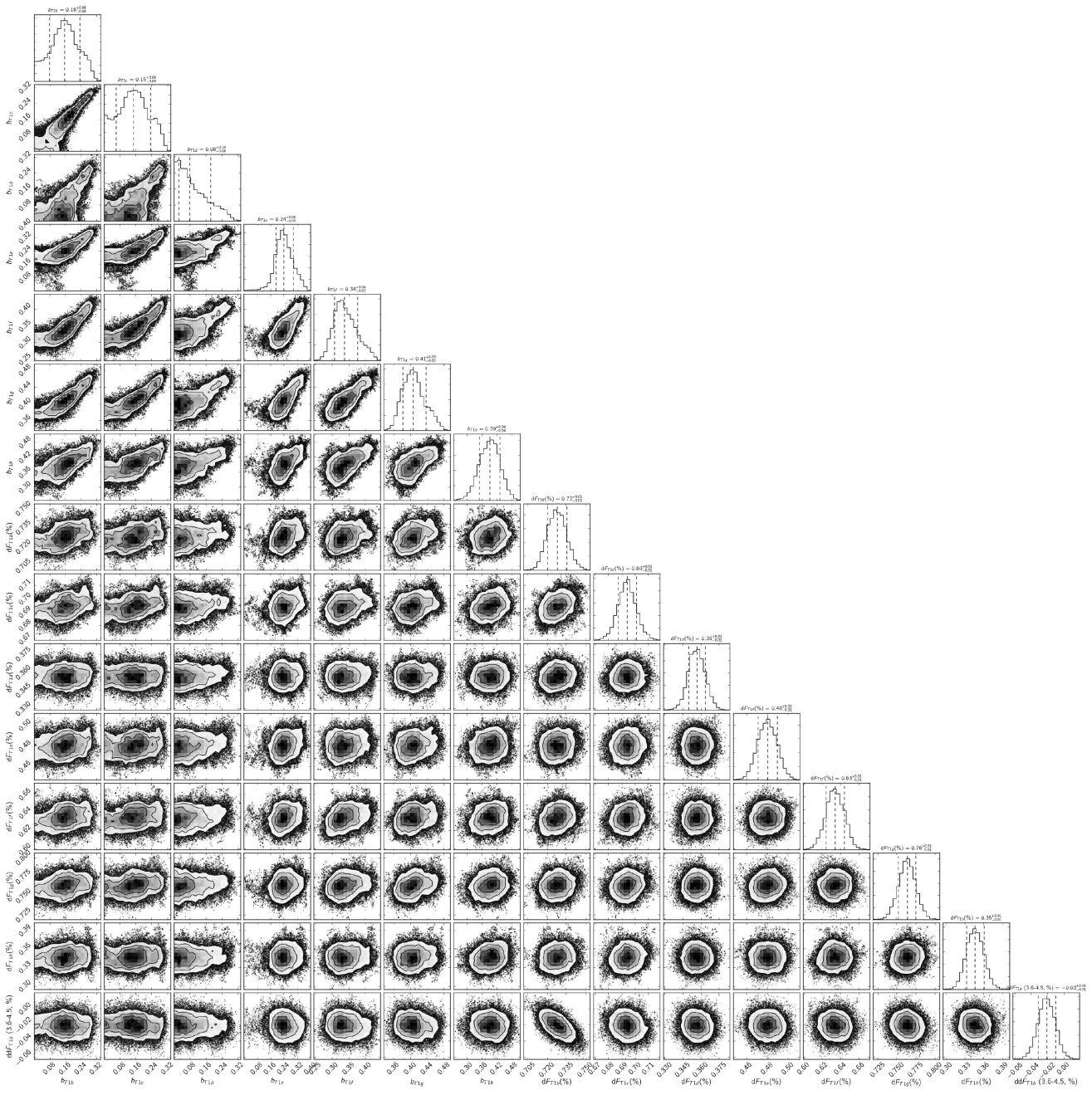

Figure B7. Cross-correlation plots and histograms of the posterior PDFs of the transit depths and impact parameters for the seven planets, as well as the difference in transit depth of planet TRAPPIST-1b between IRAC channel 1 and channel 2.

Table B1 Median values ($\text{median}_{\text{in}}$, $\text{median}_{\text{out}}$) and median absolute deviations (σ_{in} and σ_{out}) of the residuals in and out of transit, using the residuals from the global analysis. The last column gives the significance of the difference between $\text{median}_{\text{in}}$ and $\text{median}_{\text{out}}$, computed as $\frac{|\text{median}_{\text{in}}-\text{median}_{\text{out}}|}{\sqrt{\sigma_{\text{in}}^2+\sigma_{\text{out}}^2}}$.

Planet	Epoch	$\text{median}_{\text{in}}$ (ppm)	σ_{in} (ppm)	$\text{median}_{\text{out}}$ (ppm)	σ_{out} (ppm)	Significance of the difference, σ
b (3.6 μm)	322	−188	421	213	600	0.55
	326	−371	415	33	488	0.63
	327	449	287	26	620	0.62
	330	−9	350	−107	522	0.16
	333	−107	522	151	588	0.33
	334	−27	587	143	350	0.25
	335	158	530	90	416	0.10
	338	445	637	162	761	0.29
	339	82	340	−153	334	0.49
	341	295	293	−45	421	0.66
	342	−407	635	219	579	0.73
b (4.5 μm)	78	133	420	−290	464	0.68
	86	−32	344	362	390	0.76
	93	−240	303	−192	740	0.06
	218	−265	407	350	588	0.86
	219	279	527	−318	413	0.89
	220	−386	353	194	550	0.89
	222	−406	583	90	570	0.61
	224	104	519	−240	659	0.41
	225	−328	471	179	612	0.65
	226	−136	372	196	480	0.55
	227	−512	354	−361	621	0.21
	228	192	279	−188	423	0.75
	229	−226	831	−296	338	0.08
	230	−242	732	−684	624	0.46
	231	89	979	122	384	0.03
	318	−59	382	−430	606	0.52
	320	182	379	−67	473	0.41
	321	−229	466	−27	669	0.25
	324	226	417	14	561	0.30
	325	208	553	199	538	0.01
	328	−145	700	110	530	0.29
	332	−45	530	−259	617	0.26
	336	334	669	−41	1003	0.31
	340	359	770	368	362	0.01
c	70	126	475	11	618	0.15
	71	242	302	−171	404	0.82
	152	−331	251	−645	360	0.71
	153	102	405	−85	701	0.23
	154	512	538	75	964	0.40
	155	345	623	−11	658	0.39
	156	−92	684	53	596	0.16
	157	−167	742	−400	794	0.21
	158	−89	371	−311	750	0.27
	159	201	653	−168	391	0.48
	160	−112	380	−113	780	0.00
	215	124	602	−264	379	0.55
	216	340	664	−165	676	0.53
	217	−233	536	259	779	0.52
	218	13	547	−82	612	0.12
	219	83	721	−79	452	0.19
	220	−32	472	96	670	0.16
	221	−208	711	18	398	0.28
	222	333	501	−126	576	0.60
	223	−241	509	286	614	0.66
	224	90	772	−43	560	0.14
	225	−229	561	−79	376	0.22
	226	−71	602	−179	588	0.13
	227	−93	556	−297	734	0.22
	228	345	777	−98	333	0.52
	229	14	507	−128	466	0.21

Table B1 – *continued*

Planet	Epoch	median$_{in}$ [ppm]	σ_{in} [ppm]	median$_{out}$ [ppm]	σ_{out} [ppm]	Significance of the difference [σ]
	230	399	746	−115	559	0.55
d	−4	−159	754	260	733	0.40
	−3	110	472	112	551	0.00
	−2	−59	849	−103	674	0.04
	−1	61	593	−5	409	0.09
	0	−83	538	−96	669	0.02
	33	45	580	−63	721	0.12
	34	−73	511	180	579	0.33
	35	−87	723	23	451	0.13
	36	157	428	185	478	0.04
	37	313	652	−118	478	0.04
	38	−18	727	189	656	0.21
	39	−131	320	292	425	0.80
	40	312	720	206	573	0.12
	41	54	617	191	646	0.15
e	−1	−128	627	159	763	0.29
	0	−316	487	87	540	0.55
	24	218	500	−257	446	0.71
	25	−257	446	−49	693	0.25
	26	−149	637	234	559	0.45
	27	234	606	−392	508	0.79
	28	−201	695	334	580	0.59
	29	−251	531	−5	736	0.27
f	−2	−235	635	27	512	0.32
	−1	195	440	31	560	0.23
	0	40	632	159	726	0.12
	15	−205	516	−307	793	0.11
	16	−274	641	188	493	0.57
	17	−117	571	−203	612	0.10
	18	79	621	−196	541	0.33
g	−1	−235	635	−230	525	0.01
	0	555	531	377	557	0.23
	12	−48	336	+199	735	0.31
	13	−165	611	209	334	0.54
	14	143	609	−365	501	0.64
h	0	14	459	−26	646	0.05
	9	−27	540	−155	557	0.16

This paper has been typeset from a TEX/LATEX file prepared by the author.